



Title	Plasmonic surface nanostructuring of Au-dots@SiO ₂ via laser-irradiation induced dewetting
Author(s)	Yu, Ruixuan; Shibayama, Tamaki; Ishioka, Junya; Meng, Xuan; Lei, Yanhua; Watanabe, Seiichi
Citation	Nanotechnology, 28(27), 275701 https://doi.org/10.1088/1361-6528/aa74f7
Issue Date	2017-07-07
Doc URL	http://hdl.handle.net/2115/70924
Rights	This is an author-created, un-copyedited version of an article accepted for publication in Nanotechnology. The publisher is not responsible for any errors or omissions in this version of the manuscript or any version derived from it. The Version of Record is available online at http://iopscience.iop.org/article/10.1088/1361-6528/aa74f7 .
Type	article (author version)
File Information	Revised Manuscript_20170502-R2_clear.pdf



[Instructions for use](#)

1 **Plasmonic Surface Nanostructuring of Au-dots@SiO₂ via**

2 **Laser-Irradiation Induced Dewetting**

3
4 Ruixuan Yu¹, Tamaki Shibayama¹, Junya Ishioka¹, Xuan Meng^{1,2}, Yanhua Lei¹, and Seiichi Watanabe¹

5 ¹Center for Advanced Research of Energy and Materials, Faculty of Engineering, Hokkaido University,
6 Sapporo, Hokkaido 060-8628, Japan

7 ²School of Nuclear Science and Technology, Lanzhou University, Lanzhou 730000, China

8 E-mail: (T. Shibayama) shiba@qe.eng.hokudai.ac.jp

9 10 11 Abstract

12 The in-situ observation of Au dot formation and the self-assembly dynamics of Au nanoparticles (NPs) was
13 successfully demonstrated via dewetting of Au thin films on SiO₂ glass substrates under nano-second pulsed
14 laser irradiation using a multi-quantum beam high-voltage electron microscope. Moreover, using electron
15 energy-loss spectroscopy (EELS) performed in a scanning transmission electron microscope (STEM), the
16 plasmonic properties of the formed Au/SiO₂ nanostructure were analyzed to demonstrate its validity in
17 advanced optical devices. The uniformly distributed Au NPs evolved into a dot alignment through movement
18 and coalescence processes was demonstrated in this in-situ observation. We carried out the Plasmon-loss images
19 of the plan view and the cross-section of the Au/SiO₂ nanostructures were obtained at the plasmon-loss peak
20 energy for investigate the three-dimensional distribution of surface plasmon. Furthermore, discrete-dipole
21 approximation (DDA) calculations were used to simulate the plasmonic properties, such as the surface plasmon
22 resonance and the surface plasmon field distribution, of isolated single Au/SiO₂ nanostructures. This STEM-
23 EELS-acquired surface plasmon map of the cross-sectional sample is in excellent agreement with the DDA

1 calculations. This results demonstrated the influence of the contact condition between Au NP and SiO₂ glass on

2 the plasmonic properties, and may improve the technology for developing advanced optical devices.

3

4

1 **1. Introduction**

2 The direction and periodic intervals of femtosecond- or nanosecond-pulsed laser-induced periodic
3 surface structures (LIPSS) strongly depend on the wavelength and electric field vector (E vector) of
4 the incident laser [1, 2]. Recently, we successfully obtained LIPSS via nanosecond-pulsed laser
5 irradiation and via Ar^+ ion and nanosecond-pulsed laser co-irradiation on an Au thin film deposited
6 on SiO_2 glass substrates [3, 4]. Also, the obtained direction of the LIPSS was either parallel [1, 3] or
7 perpendicular [2, 4] to the E vector of the incident laser.

8 Recently, transmission electron microscope (TEM) in situ observations of thermal annealing-
9 induced [5] or pulsed laser-induced [6, 7] dewetting of metallic films deposited on a dielectric
10 substrate was obtained during the assembly process of the metallic films into a nanoparticle (NP)
11 array. These results have demonstrated that in situ observation using a modified TEM is an effective
12 method to study the thermal annealing- or quantum beam irradiation-induced dewetting. However, in
13 situ observational research capturing the NP array variation as a function of increased laser pulse is
14 as yet insufficient. In previous works, we have reported in situ observation of nanosecond-pulsed
15 irradiation-induced dewetting evolution of an Au film on an SiC substrate using a high-voltage
16 electron microscope (HVEM) equipped with a nanosecond-pulsed laser [8].

17 Noble metallic NPs exhibit the well-known quantum phenomena of surface plasmon resonance
18 (SPR), which is a collective oscillation of conduction electrons driven by the incident light. The SPR
19 can enhance the electronic field surrounding the noble metallic NPs, which is capable of enhancing
20 the performance of biosensors [9], photocatalytics [10-12] and solar cells [13, 14]. The desired SPR
21 frequency of a noble metallic NP/dielectric system can be produced by controlling the size [15, 16],
22 shape [16] and interparticle distance [17] of the noble metallic NPs. Therefore, clarifying the

1 mechanism underlying the noble metallic NP formation can be the key to controlling the morphology
2 and distribution of the noble metallic NPs, and ultimately to tailoring the SPR properties.

3 We have previously investigated the photoabsorption spectrum of the formed noble metallic
4 NP/dielectric systems to analyze the plasmonic properties of the SPR induced by the incident light
5 [3, 4, 18-21]. Additionally, we have used discrete-dipole approximation (DDA) calculations to
6 understand the incident light-induced optical properties and the surface plasmon distribution of the
7 Au NP/SiO₂ nanostructures [21]. In these results, generally the wavelengths of the SPR peak red shifts
8 are in good agreement with the increase in the mean diameter of the Au NPs on the SiO₂ substrates
9 [3, 4, 18-21]. However, the formation of LIPSS as a result of co-irradiation with Ar⁺ ions and a
10 nanosecond-pulsed laser leads to unexpected SPR peak blue shifts as the mean diameter of the Au
11 NPs on the SiO₂ substrates increases [4]. This unexpected SPR peak blue shift is possibly owing to
12 the effects of the charge distribution around the Au NPs resulting from the relative differences in the
13 distances between the Au NPs formed by LIPSS [4, 17]. However, it is difficult to obtain the surface
14 plasmon distribution around the Au NPs using photoabsorption spectroscopy. Electron energy-loss
15 spectroscopy (EELS) performed in a scanning TEM (STEM), however, enables mapping of the
16 distribution of electrically excited surface plasmons of metallic nanostructures [22-26]. The surface
17 plasmon modes and distribution can be influenced by changes in the shape [22-24], size [26] and
18 interparticle distance [25] of the metallic nanostructures. The results of the STEM-EELS experiment
19 were in excellent agreement with theoretical calculations from methods such as the boundary element
20 method [23-27]. Therefore, using STEM-EELS experiments and theoretical calculations it is possible
21 to probe the unique plasmonic properties in periodic metallic NP/dielectric nanostructures.

22 In this study, the in-situ observation experiment successfully demonstrated the Au dot formation

1 and the self-assembly dynamics of Au nanoparticles (NPs) via nanosecond-pulsed laser irradiation-
2 induced dewetting of Au thin films on an SiO₂ glass substrate using a multi-quantum beam HVEM
3 (MQB-HVEM), which can be developed the control technology of laser induced dewetting. We
4 successfully observed the initial process of LIPSS formation using a MQB-HVEM, and investigated
5 the plasmonic properties of the formed Au/SiO₂ nanostructures via STEM-EELS. We carried out the
6 plasmon-loss images of the plan view and the cross-section of the Au/SiO₂ nanostructures were
7 performed at the plasmon-loss peak for investigating the three-dimensional distribution of surface
8 plasmon. Moreover, we compared the results for the plasmonic properties of the Au/SiO₂
9 nanostructures obtained from both DDA calculations and STEM-EELS experiments. The above
10 results demonstrated the formed Au/SiO₂ nanostructures validity in advanced optical devices, and
11 may improve the technology for developing advanced optical devices.

12

13 **2. Experimental procedure**

14 The SiO₂ glass substrates with a diameter of 10 mm and a mirror finish on both sides (Shin-Etsu
15 Chemical Co., Ltd., Tokyo, Japan, O-H density: 501 ppm, dielectric constant: 3.9) were used in ex
16 situ irradiation experiments. The in situ samples were cut from the same SiO₂ glass substrates used
17 for the ex situ samples, where the cut pieces were mechanical thinned from the back surface up to a
18 thickness of 0.03 mm. The TEM samples were prepared by Ar⁺ ion polishing from the back surface
19 at an angle of 5 degrees using a precision ion polishing system (PIPS; Gatan Co., Ltd., CA, USA).
20 The Au thin films were simultaneously deposited on the ex situ and in situ samples (mirror surface)
21 using a vacuum evaporator at room temperature by electrically heating the Au source (purity, 99.9%)
22 operated at a pressure of 7.0×10^{-3} Pa.

1 In this study, the in situ irradiation experiments were performed in a MQB-HVEM (JEOL, JEM-
2 ARM1300, Tokyo, Japan) equipped with a nanosecond-pulsed laser (Inlite II, Continuum Co., Ltd.,
3 CA, USA). The nanosecond-pulsed laser operated at a wavelength of 532 nm with a nominal pulse
4 duration of 5–7 ns and a repetition rate of 2 Hz. The nanosecond-pulsed laser was irradiated onto the
5 surface of the Au thin film on the SiO₂ glass substrate at an angle of 44 degrees. A video of the laser-
6 induced dewetting was recorded using the bottom-mounted charge-coupled device (CCD) camera of
7 the MQB-HVEM at a frame rate of 10 frames per second (HD video software: Gatan
8 DigitalMicrograph, Ver. 2.30.542.0, video formats: *.mpeg4). Because this in situ experimental
9 apparatus does not have a synchronized system between the sequential CCD frames and the laser
10 pulses, we determined that a frame exhibiting a microstructure change when compared to a previous
11 frame was obtained just after a laser strike. We also confirmed that every five frames after this initial
12 laser strike frame exhibited some change in the microstructure caused by the laser irradiation. Further,
13 the ex situ irradiation experiments and nanosecond-pulsed laser energy density measurements were
14 performed using an ex situ experimental apparatus, wherein the laser was irradiated perpendicular to
15 the surface of the Au thin film on the SiO₂ glass substrate. The average laser energy density was 50
16 mJ/cm².

17 After the ex situ irradiation, photoabsorbance measurements were performed with a
18 spectrophotometer (JASCO, V-630, Tokyo, Japan) using an aperture with a diameter of 0.1 mm to
19 confine the irradiated region. The surface morphology of the samples was observed by SEM (JEOL,
20 JSM-7001FA, Tokyo, Japan), and cross-sectional microstructural analyses were performed via TEM
21 (FX-TEM; JEOL, JEM-2000FX). The EELS analyses were performed via a spherical aberration-
22 corrected STEM (Cs-STEM; FEI, Titan G2 60-300) equipped with an electron monochromator, which

1 improves the electron energy resolution to about 0.12 eV (defined by the full width at half maxima
2 of the zero-loss peak). To analyze the peak occurring in the EELS spectrum, we using the Gaussian
3 non-linear least squares (NLLS) fitting, Zero-loss peak removal and background removal via the
4 DigitalMicrograph (Ver. 2.11.1404.0) software. Cross-sectional TEM samples for the FX-TEM and
5 the spherical aberration-corrected TEM/STEM (Cs-TEM/STEM; FEI, Tital G2 60-300) were
6 prepared using focused ion beam equipment (FIB; JEOL, JEM-9320).

7 In this study, the DDA method was applied to calculate the photoabsorption coefficients and the
8 surface plasmon near-field distribution of the Au NPs on the SiO₂ glass substrate, using the software
9 package DDSCAT 7.3 developed by Draine and Rlatau [28, 29]. In addition, the Meng et al. [21]
10 modified model of an Au NP on a hemispherical SiO₂ glass substrate was used for the DDA
11 calculation in this work. The wavelength-dependent dielectric function of bulk Au extracted from
12 Johnson et al. [30] was used, as was the dielectric constant (3.9) of the SiO₂ glass substrate. After the
13 DDA calculation, a schematic illustration of the 3D model of the Au NP on the surface of the SiO₂
14 glass substrate was obtained by Paraview 4.4.0 [31].

15

16 **3. Results and Discussion**

17 Figure 1(a) shows an SEM image of the surface morphology of the ex situ sample, where the
18 surface can be seen to exhibit an uneven covering of Au granular grains on the as-deposited Au thin
19 films on the SiO₂ glass substrate. The cross-sectional sample was prepared from the as-deposited ex
20 situ sample using FIB equipment, and from the cross-sectional FX-TEM image (Figure 1(b)), the
21 thickness of the Au thin films are seen to be approximately 15 nm thick. In these FX-TEM
22 observations, the areas that appear thinner than the other regions may be the crack-like structures seen

1 in Figure 1(a). Figure 1(c) shows an FX-TEM image of the surface morphology and a selected area
2 diffraction pattern of the in situ sample, where the same Au granular grains can be observed on the
3 surface of the as-deposited Au thin films on the SiO₂ glass substrate of the in situ sample as seen on
4 the ex situ sample. The selected area diffraction pattern confirms the as-deposited Au thin films to be
5 polycrystalline. Therefore, the Au thin film is considered to be uniform and with a thickness of
6 approximately 15 nm.

7 First, we carried out ex situ irradiation experiments to investigate the optical properties by visible
8 optical absorption spectra. Figure 1(d) and (e) show a surface morphology SEM image and a cross-
9 sectional Cs-TEM image, respectively, of the irradiated ex situ sample obtained after 10 pulses. After
10 10 pulses of irradiation, the aspect ratio of the diameter/height of the formed Au NP is about 1.18,
11 and the contact angle between the Au NP and the SiO₂ glass substrate is $\theta_1=143.8^\circ$. This contact angle
12 is consistent with the classical contact angle between a liquid Au NP and an SiO₂ glass substrate [32].
13 Figure 1(f) shows the visible optical absorption spectrum of the irradiated ex situ sample after 10
14 pulses, exhibiting a clear peak corresponding to an SPR-enhanced absorption at a wavelength of 537
15 nm (photon energy: 2.31 eV). These results demonstrate that, after laser irradiation with an average
16 energy density of 50 mJ/cm² for 10 pulses, Au NPs are formed on the surface of SiO₂ glass substrate
17 that demonstrate some SPR effect. Therefore, these laser parameters were used to perform the in situ
18 observation experiment.

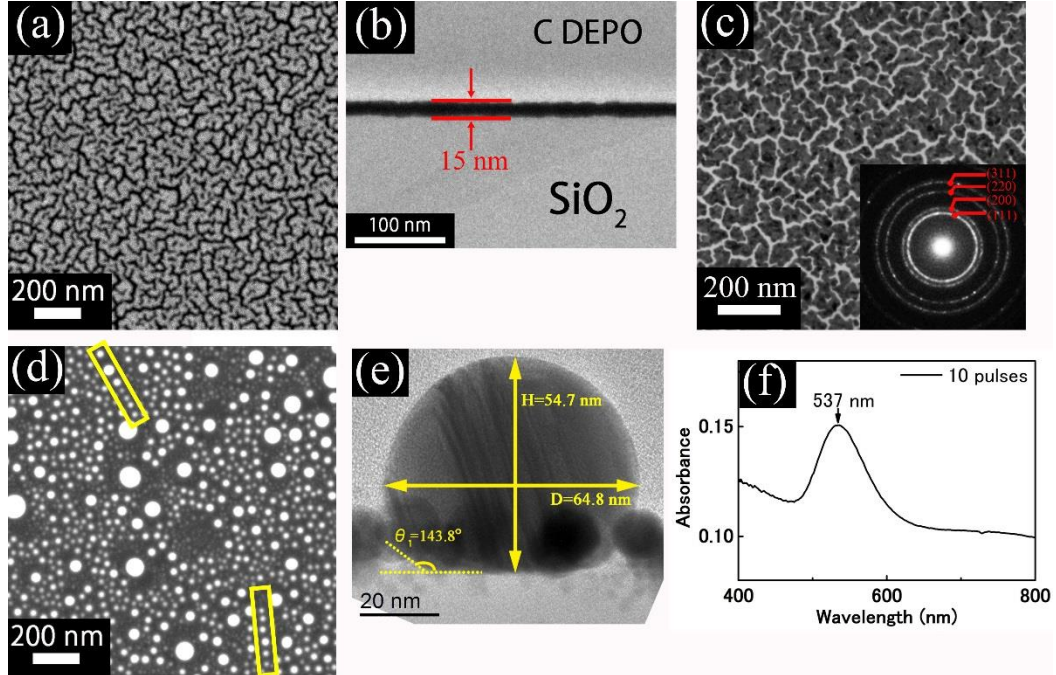


Figure 1. (a) SEM and (b) cross-sectional FX-TEM images obtained before irradiation of the ex situ sample. (c) Surface FX-TEM image and selected area diffraction pattern of the in situ sample. (d) SEM and (e) cross-sectional Cs-TEM images obtained after 10 irradiation pulses on the ex situ sample. (f) Visible optical absorption spectrum obtained after 10 irradiation pulses on the ex situ sample.

1 Generally, dewetting on the surface of a dielectric substrate is accomplished by a process wherein,
 2 first, hole formation occurs in the metallic thin films; second, hole growth progresses; third, ligament
 3 breakup occurs; and finally, metallic NPs are formed [6, 33]. Yang et al. have made very well ordered
 4 surface nanopatterns of Au and Ag NPs by using temple-confined dewetting process [34].
 5 McKeown et al. have observed the progression of a metallic film into an NP array by in situ
 6 nanosecond-pulsed laser irradiation [6, 7]. Further, increasing the number of laser pulses can induce
 7 the arrangement of the Au NPs to change and the formation of LIPSS to occur at suitable conditions
 8 [3, 4]. As shown in Figure 1(d), several Au NPs in the yellow box are in a line-like arrangement.
 9 Figure 2 show the dewetting process of the in situ sample during the in situ nanosecond-pulsed laser
 10 irradiation experiment with a varying number of laser pulses, where the images are obtained from the

1 video test by MQB-HVEM (The video of the in situ observation running from before irradiation until
2 600 irradiation pulses is available in the Supplementary Information, Video M1). Immediately after
3 the initial irradiation pulse, the Au thin films change to Au NPs possessing diameters from a few tens
4 to a few hundreds of nanometers (Figure 2(b)). After two irradiation pulses, some of the Au NPs
5 vanish from the view of the in situ observation, which we hereafter call the “vanished Au NPs.” In
6 addition to the occurrence of vanished Au NPs, movement, coalescence and growth of the remaining
7 Au NPs were observed. In this in situ observation experiment, after 600 irradiation pulses the size,
8 shape and distribution of the Au NPs are likely to stabilize. Therefore, we analyzed the behavior of
9 the movement, coalescence and distribution of the Au NPs as a function of irradiation up to 600
10 irradiation pulses. As shown in Figure 2, the behavior of the Au NPs is analyzed using the in situ
11 MQB-HVEM images, analyzing consecutive images for Au NPs movement (blue arrows),
12 coalescence and growth (red arrows), and vanished Au NPs (orange dotted circle) as the number of
13 laser pulses is increased. (The comparison of different MQB-HVEM images obtained after different
14 numbers of laser pulses, the image processing method and the results are displayed in Supporting
15 Information S1.) In this in situ observation experiment, the vanished Au NPs often occur in the area
16 enclosed by yellow dotted lines in Figure 2. These vanished Au NPs may disappear owing to laser
17 ablation, and based on these results, we consider this area to be one that experiences a high laser
18 energy. In this high-laser-energy area, the number of Au NPs decreases because several Au NPs
19 vanish or move to both sides (yellow dotted line in Figure 2), where the Au NPs ultimately develop
20 into a line-like arrangement (analysis method displayed in Supporting Information S2).

21 The evolution of the size and shape of the Au NPs was also analyzed as a function of increasing
22 number of laser pulses using the TEM images of the in situ observation. Figure 3(a) plots the average

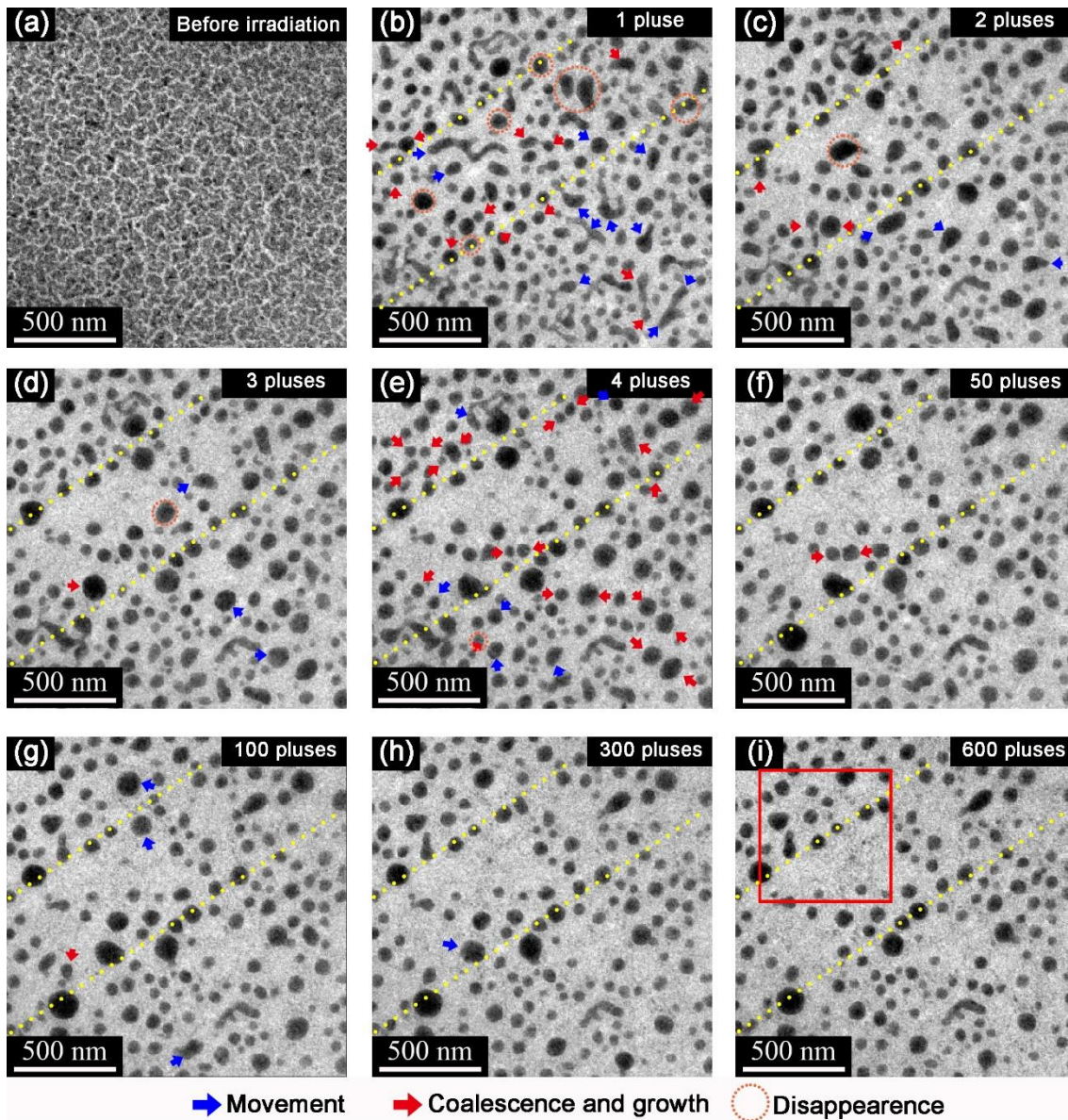


Figure 2. In situ observation of nanosecond-pulsed laser irradiation-induced dewetting of the in situ sample obtained (a) before irradiation and obtained after laser irradiation for (b) 1, (c) 2, (d) 3, (e) 4, (f) 50, (g) 100, (h) 300 and (i) 600 pulses. Each still image was extracted from the video of the in situ observation recorded by CCD camera (video formats: *.mpeg4). Marks indicate Au NPs that have moved (blue arrows), coalesced and grown (red arrows), and vanished (orange dotted circle) with increased number of laser pulses.

1 Heywood diameter and average aspect ratio of the Au NPs with respect to the number of laser
2 pulses. After 1 irradiation pulse, the average Heywood diameter of formed Au NPs is 60.1 ± 1.2 nm.
3 In this study, as the number of pulses increases from 1 to 10, the average Heywood diameter increases
4 and simultaneously the average aspect ratio suddenly decreases. After 10 irradiation pulses, the
5 average Heywood diameter is maximized (65.9 ± 1.5 nm) for this in situ observation experiment. As
6 the number increases from 10 to 600 irradiation pulses, the average Heywood diameter decreases to
7 60.4 ± 1.2 nm while the aspect ratio, which initially exhibits a slight fluctuation, ultimately stabilizes
8 at a value of 1.2 in this in situ observation experiment. The average Heywood diameter of Au NPs
9 after 1 and 600 irradiation pulses are close. However, the distribution of the average Heywood
10 diameter of Au NPs are different between them. As increasing laser irradiation pulses, the histogram
11 is getting to show Gaussian distribution and highest frequency of Heywood diameter of Au NPs is
12 going toward into the average value.

13 Figure 3(c) shows the extended MQB-HVEM image obtained from an area marked by a red square
14 in Figure 2(i). Because of the higher point–point resolution in the MQB-HVEM image than is
15 available in the video of the in situ observation, many small Au NPs are observed herein than was
16 possible in the video. The Heywood diameter histogram of the small Au NPs is show in Figure 3(d),
17 exhibiting an average of 6.5 ± 0.1 nm. Therefore, the movement process of the larger Au NPs could be
18 achieved through coalescence around these small Au NPs.

19 Generally, LIPSS are formed as a result of the interference between the incident laser light and the
20 scattered laser light induced by defects or unevenness of the substrate surface [1-4]. Longstreth-Spoor
21 et al. [35] have investigated the periodic surface nanostructures of Co on Si substrates by two-beam

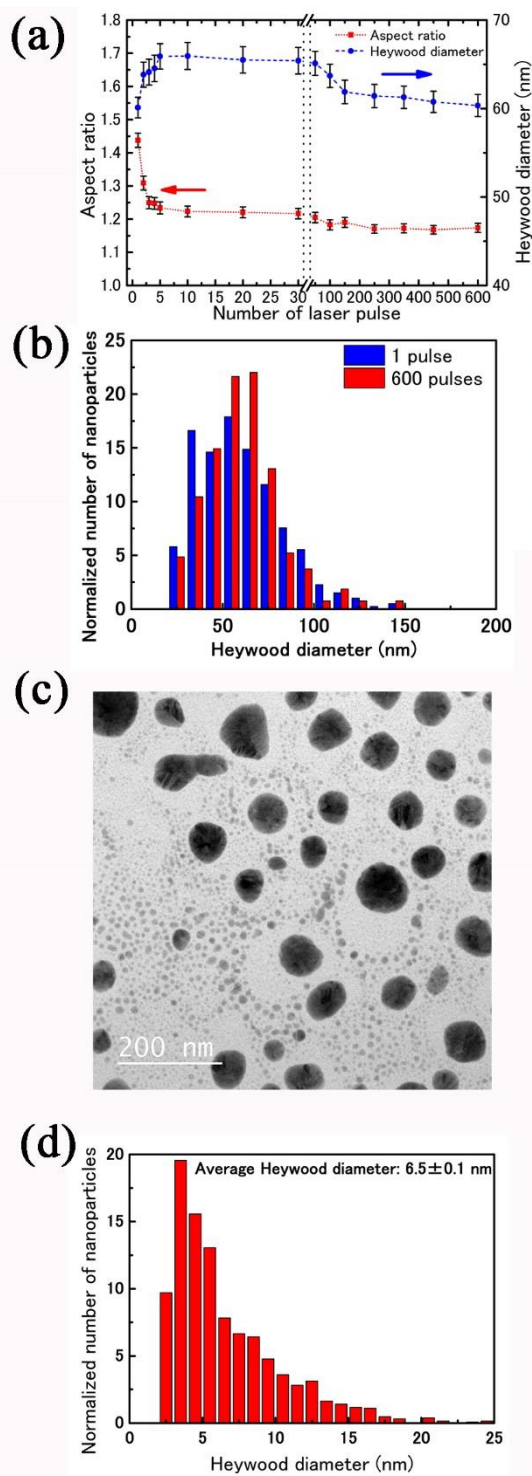


Figure 3. (a) Average Heywood diameter (equivalent circle diameter) and average aspect ratios of the Au NPs as a function of the number of laser pulses. Error bars indicate the standard error. (b) Histogram of the Heywood diameters obtained from the in situ TEM image in Fig. 2(b). (c) High-magnification MQB-HVEM image obtained after the in situ observation of the area in the red square in Fig. 2(i). (d) Histogram of the Heywood diameters of these small Au NPs observed in Fig. 3(c).

1 laser interference irradiation, where small Co NPs formed in regions of constructive interference
2 (high temperature regions) and large Co NPs formed in regions of destructive interference (low
3 temperature regions) [35]. Recently, we examined nanosecond-pulsed laser irradiation [3] as well as
4 Ar^+ ion and nanosecond-pulsed laser co-irradiation [4] upon Au thin films deposited on SiO_2 glass
5 substrates. Therein, initially the Au NP formation was dispersed uniformly, and as the irradiation dose
6 was increased, ultimately the LIPSS formed on the SiO_2 glass substrate. In that study, however, we
7 inadequately explicated the process underlying the change of the uniformly dispersed Au NPs to
8 LIPSS.

9 From the result of this study, we now reconsider the LIPSS formation process. Under single-beam
10 laser irradiation and based on the interference between the incident laser light and the scattered laser
11 light, the energy density was periodically distributed on substrate surface. In the regions of
12 constructive interference, some of the Au NPs vanish by laser ablation while some move to regions
13 of destructive interference. Therefore, on the surface of substrate, the number of Au NPs will decrease
14 in regions of constructive interference and will increase in regions of destructive interference. Finally,
15 randomly-dispersed Au NPs change to a periodic nanostructure.

16 From the results of the in situ observation, we record the dewetting behavior of Au thin films on
17 SiO_2 glass substrates during nanosecond-pulsed laser irradiation and analyzed the change of the
18 Heywood diameter and the aspect ratio. We also carried out STEM-EELS experiments to investigate
19 the plasmonic properties of the formed Au NPs induced by laser irradiation.

20 Figure 4 show the results of the STEM-EELS experiment on the in situ sample. Figure 4(a)
21 shows a Cs-TEM image of the in situ sample surface after 600 irradiation pulses, and Figure 4(b)
22 shows the EELS spectrum for an incident electron beam at a point near an Au NP on the in situ

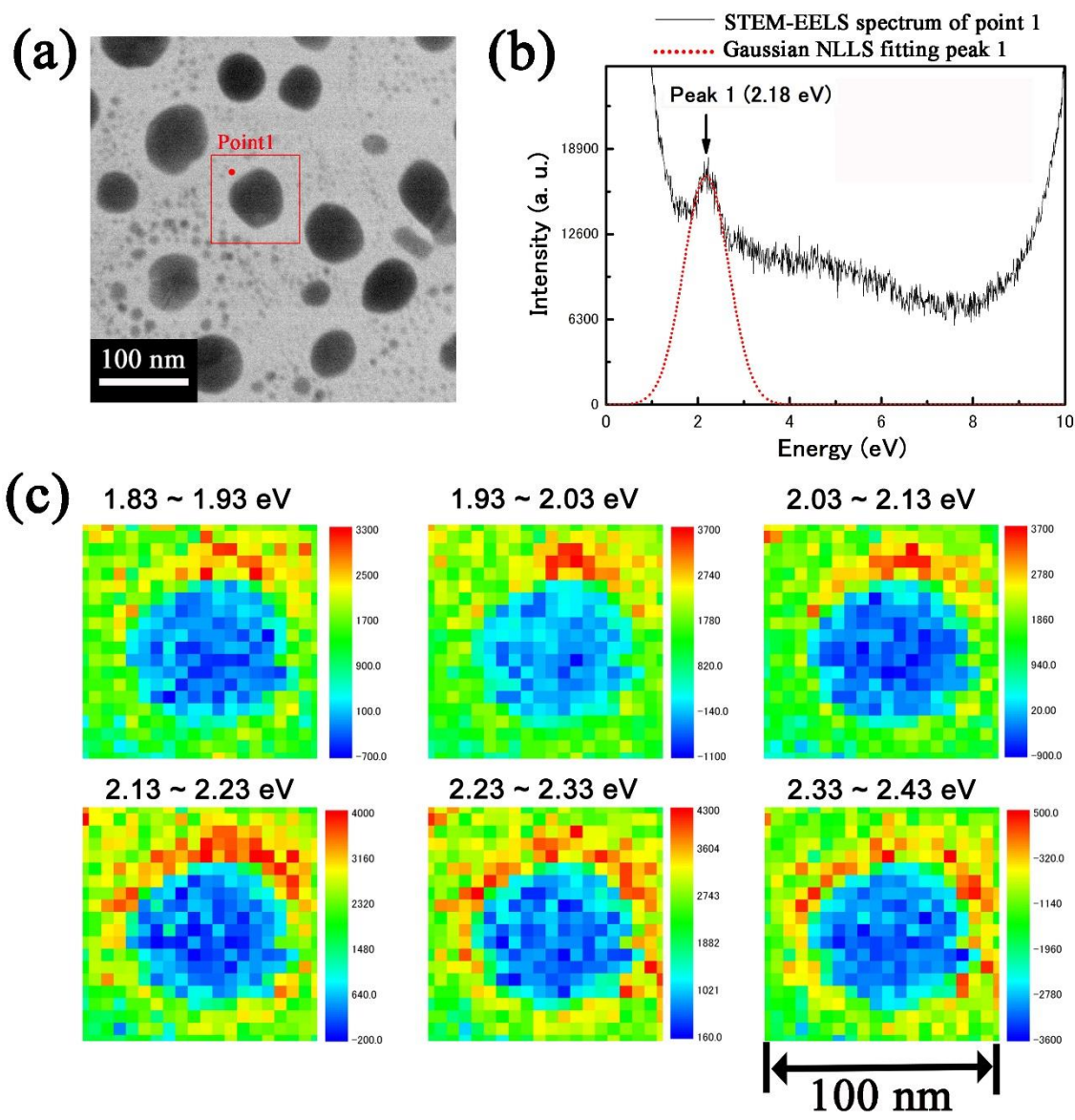


Figure 4. (a) Cs-TEM image of the in situ sample obtained after 600 irradiation pulses. (b) Extracted experimental STEM-EELS spectrum for an incident electron beam at point 1 marked in (a). (c) Surface plasmon map obtained from the measured STEM-EELS excitation intensity at the area in the red square in (a) with an energy selection slit at 0.1 eV from 1.83 to 2.43 eV and a mesh dimension of $5 \times 5 \text{ nm}^2$.

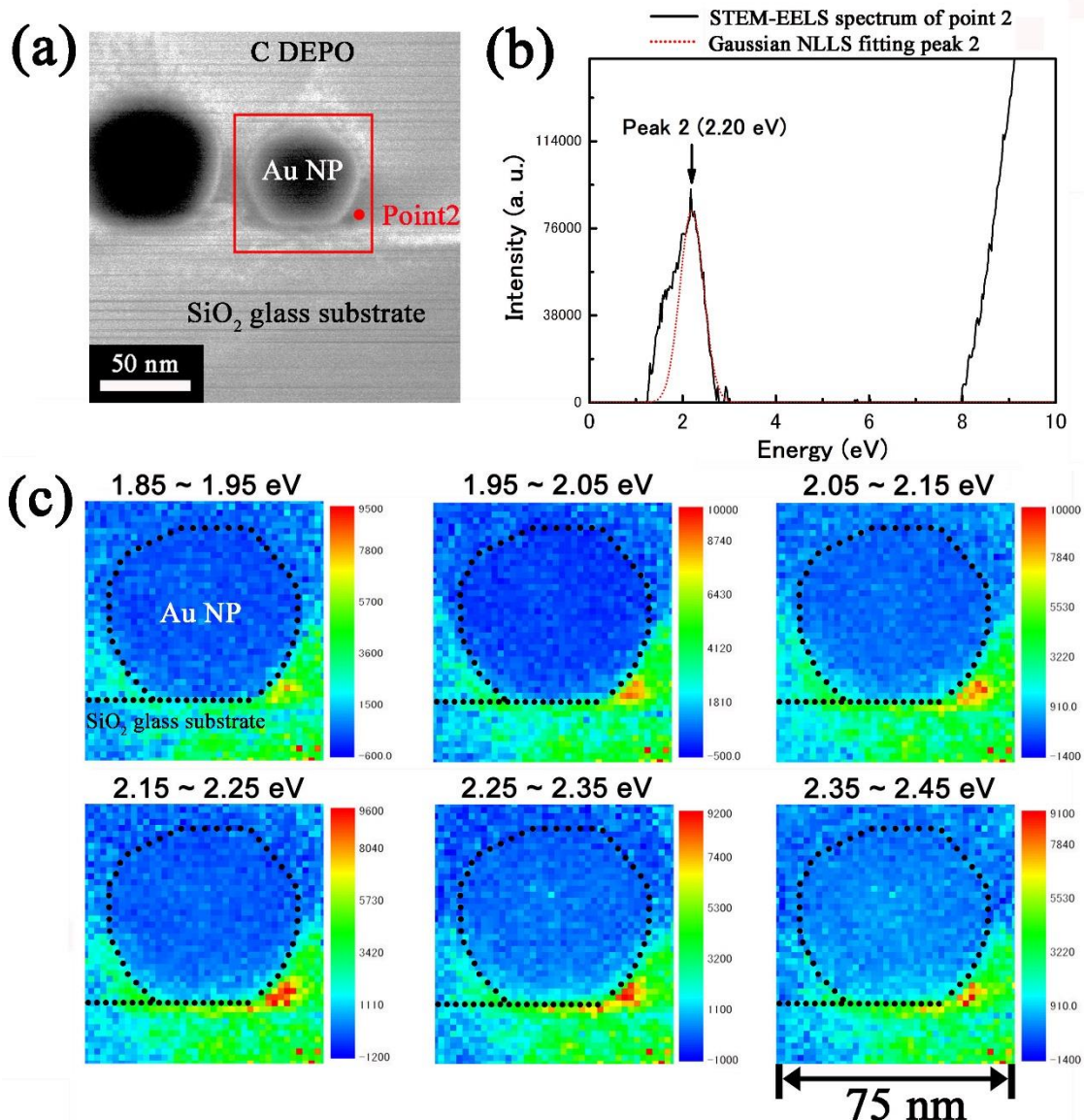


Figure 5. (a) Cross-sectional Cs-TEM image obtained after 7500 irradiation pulses for the sample described in Ref.⁴. (b) Extracted experimental STEM-EELS spectrum for an incident electron beam at point 2 marked in (a). (c) Surface plasmon map obtained from the measured STEM-EELS excitation intensity at the area in the red square in (a) with an energy selection slit at 0.1 eV from 1.85 to 2.45 eV and a mesh dimension of $2 \times 2 \text{ nm}^2$.

1 sample (labeled point 1 in Figure 4(a)). The EELS spectrum exhibits a clear peak corresponding
2 to the plasmon loss peak (labeled peak 1 in Figure 4(b)). After Gaussian NLLS fitting of the peak
3 via DigitalMicrograph, we obtained a plasmon loss energy of 2.18 eV. This plasmon loss energy is
4 close to the reported plasmon loss peak of Au nanostructures obtained by Chu et al. [22-23].

5 Therefore, a surface plasmon map was obtained by mapping the STEM-EELS excitation intensity
6 from an area including an Au NP (square area in Figure 4(a)) with an energy selection slit at 0.1 eV
7 and ranging from 1.93 to 2.43 eV (Figure 4(c), mesh dimension of $5 \times 5 \text{ nm}^2$). As shown in Figure
8 4(c), the near-field distribution of the surface plasmons surrounding the Au NP is demonstrated.

9 In our previous study, we reported that the Au NPs formed on the SiO_2 glass substrate were induced
10 by nanosecond-pulsed laser irradiation in the vacuum chamber [4]. Moreover, we demonstrated
11 therein via cross-sectional TEM images that an Au NP formed on the surface of the SiO_2 glass
12 substrate [4]. In this work, a cross-sectional Cs-TEM image of the same cross-sectional sample
13 prepared for use in our previous study is shown in Figure 5(a). To investigate the cross-sectional
14 plasmonic properties of the Au/ SiO_2 nanostructures in this cross-sectional sample, we obtained
15 surface plasmon maps by mapping the STEM-EELS excitation intensity. Figure 5(b) shows the EELS
16 spectrum for an incident electron beam at a point near an Au NP on the cross-sectional sample (labeled
17 point 2 in Figure 5(a), zero-loss peak and background of EELS spectrum was removed), where the
18 EELS spectrum has a clear peak corresponding to a plasmon loss peak (labeled peak 2 in Figure 5(b))
19 whose energy, by Gaussian NLLS fitting, was found to be 2.20 eV. Therefore, the surface plasmon
20 map was obtained by mapping the STEM-EELS excitation intensity from an area containing an Au
21 NP and some SiO_2 substrate (square area in Figure 5(a)) with an energy selection slit at 0.1 eV and
22 ranging from 1.85 to 2.45 eV (Figure 5(c), mesh dimension of $2 \times 2 \text{ nm}^2$). As shown in Figure 5(c),

1 the near-field distribution of the surface plasmons exists at the right and left outsides of the interface
2 between the Au NP and the SiO₂ glass substrate. In particular, the maximum STEM-EELS excitation
3 intensity is clearly present at the right outside of the interface between the Au NP and SiO₂ (Figure
4 5(c)). In previous works, we obtained Au NPs partially embedded in the SiO₂ glass substrate
5 following Ar⁺ ion irradiation [18-21] or nanosecond-pulsed laser and Ar⁺ ion co-irradiation [4], where
6 the embedded depth could be controlled by the Ar⁺ ion dose. Therefore, the cross-sectional surface
7 plasmon distribution of these partially embedded Au NPs with varying embedded depth could be
8 probed by STEM-EELS in future work.

9 As shown in Figure 5(a), the aspect ratio of the diameter/height of the Au NP is about 1.22.
10 Therefore, DDA calculations were run using this aspect ratio, and the 3D model is schematically
11 illustrated in Figure 6 of a single Au NP on the surface of an SiO₂ glass substrate in the cross-
12 sectional (X-Y plane) view (Figure 6(a)) and the top view (Y-Z plane) (Figure 6(b)). The contact
13 between the Au NP and SiO₂ glass substrate was a surface contact (Figure 6(a)), and Figure 6(c)
14 shows the DDA-calculated absorption coefficient plotted for wavelengths from 400 to 800 nm
15 (wavelength spacing of 1 nm for 500–550 nm range, and 8 nm otherwise). In this DDA calculation,
16 the incident light was along the X-direction and was polarized along the Y-direction. This
17 calculated absorption coefficient plot exhibits a clear peak at a wavelength of 525 nm (photon
18 energy: 2.36 eV), corresponding to an SPR-enhanced absorption. The simulated plasmon near-field
19 distributions were then calculated at this SPR peak wavelength (Figure 6(d)), and the color bar
20 shows the electric field enhancement $|E|^2/|E_0|^2$, where $|E_0|$ is the amplitude of the incident field and
21 $|E|$ is the amplitude of the local electric field surrounding the Au/SiO₂ nanostructure. As shown in
22 Figure 6(d), the surrounding environment of the Au NP exhibits a dipole-like plasmon field

1 distribution. In addition, regions with field enhancement up to 50 times or more exist at the outsides
2 of the interface between the Au NP and the SiO₂ glass substrate. The region of most enhancement
3 field exhibited at corners near the contacts of Au NP to the SiO₂ glass substrate is excellent
4 agreement with the STEM-EELS-acquired surface plasmon map of the cross-sectional sample
5 (Figure 5(c)). However, the simulated plasmon field distribution of left and right sides is
6 symmetrical, but the experimental cross-sectional plasmon field distribution of the left and right
7 sides is significantly different (Figure 5(c)).

8 In this study, the STEM-EELS-acquired energy of the plasmon loss peak is significantly lower than
9 the calculated photon energy of the SPR peak. A redshift (shift to the lower energy side) of the SPR
10 peak can be driven by closely-coupled metallic NPs [36, 37]. As can be seen in Figure 3(c) and 4(a),
11 following laser irradiation, a number of relatively small Au NPs a few nanometers in diameter are
12 asymmetrically dispersed around the larger Au NP. The difference existed between the experimental
13 and theoretical results in the case of the plan view STEM-EELS experiment may therefore be the
14 result of these small Au NPs. In the case of cross-sectional experiment, the plasmon loss peak could
15 be influenced by the tens of nanometers Au NP on its left side of the measured Au NP as shown in
16 Figure 5(a). Take a closer look at the Figure 5(b), a shoulder peak was observed in the lower energy
17 side of the main plasmon loss peak. For coupled Au nanostructures, it has been shown that STEM-
18 EELS can reveal the different surface plasmon distribution depending on the different surface
19 plasmon modes [23-25]. Also, the STEM-EELS can reveal the different plasmon loss peaks

1 depending on the different surface plasmon modes, and a shoulder peak can be existed when the
 2 energy of two peak are close [23-25]. Therefore, the shoulder peak as shown in Figure 5(b) could be
 3 exhibits two surface plasmon modes induced by interaction between coupled two Au NPs as show in
 4 Figure 5(a). Clarification of the shoulder peak will be an import aspect of future work. In addition,

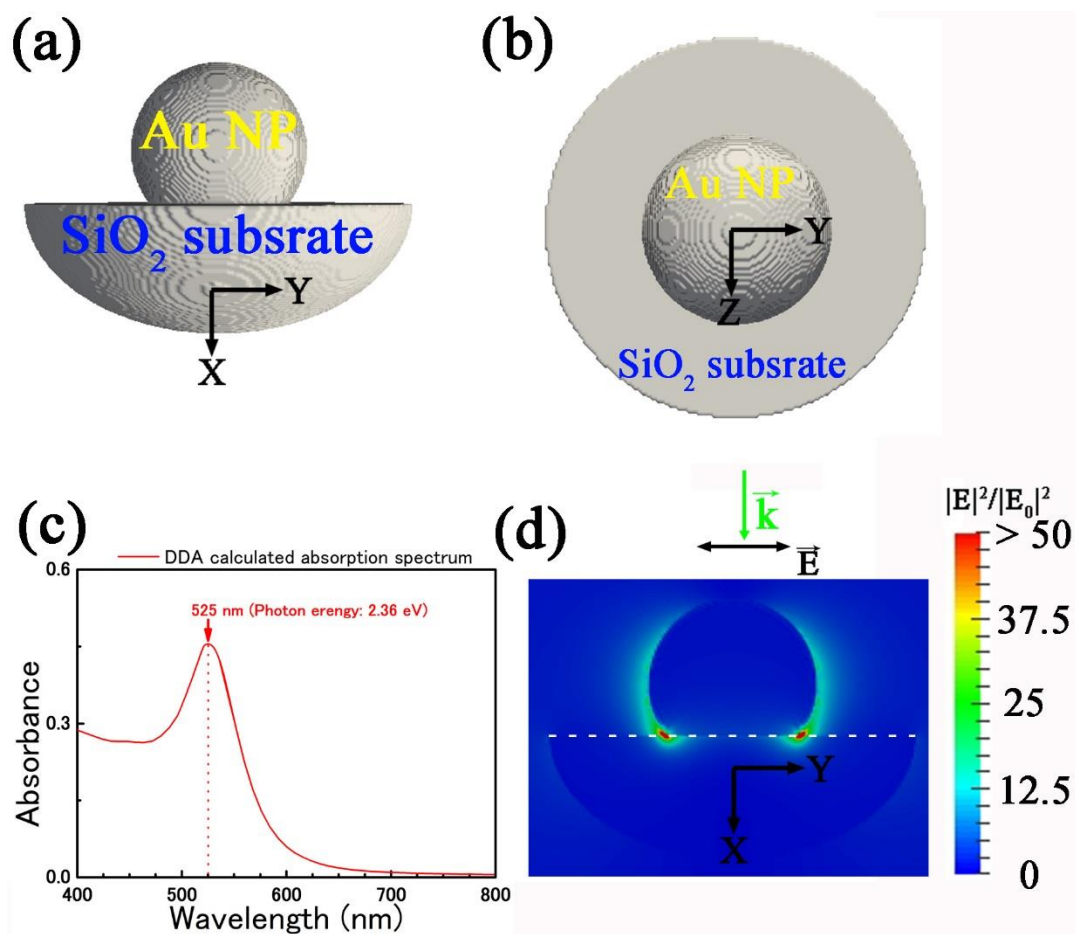


Figure 6. Schematic illustration of the 3D model used for the DDA simulation: (a) cross-sectional (X-Y plane) and (b) top-view (Y-Z plane) configuration of a single Au nanoparticle on the SiO₂ glass substrate surface. (c) DDA-calculated absorption coefficient plotted as a function of wavelength from 400 to 800 nm (wavelength spacing is 1 nm for 500–550 nm, and 8 nm otherwise). (d) Cross-sectional surface plasmon field distribution contours at the SPR peak wavelength obtained in (c). In this DDA calculation, the incident light is along the X-direction and is polarized along the Y-direction.

1 symmetrically patterned Au nanostructures exhibit a symmetric distribution pattern of the surface
2 plasmon field [23, 24]. On the other hand, Meng et al. [21] have investigated the plasmon field
3 distribution of Au NPs partially embedded in SiO₂ glass substrates at the SPR peak using the DDA
4 calculation method, where their results showed that the maximum plasmon field enhancements exist
5 at the junction regions between the Au NPs and the silica glass substrate. The plasmon field
6 distribution of metallic NPs on the dielectric is strongly influenced by contact angle between metallic
7 NPs and substrate [21, 38, 39]. The plasmon field is enhanced at corners near the contacts of Au NP
8 to the SiO₂ glass substrate could be indicated the electron oscillation on the Au NPs near the contacts
9 region [21, 38, 39]. From the above results, the plasmon field distribution of Au NP could be
10 controlled by the distribution of the Au NPs and the contact situation between the Au NPs and the
11 SiO₂ glass substrate.

12

13 **Conclusions**

14 In conclusion, using in situ observation experiments we have successfully and simultaneously
15 observed the formation of Au NPs and the modification of these Au NP shapes and arrays with
16 increasing number of laser pulses via laser irradiation-induced dewetting of Au thin films on SiO₂
17 glass substrates. The first stage (from 1 to 10 irradiation pulses) was dominated by coalescence and
18 growth, wherein the Heywood diameter of Au NPs increased. In the second stage (from 11 to 600
19 irradiation pulses), however, the Heywood diameter of Au NPs decreased. The Au NP arrays evolved
20 as the number of laser irradiation pulses increased where, through movement and coalescence, some
21 of the Au NP arrays evolved to exhibit alignment. The plasmonic properties of these Au/SiO₂
22 nanostructures formed by laser irradiation were measured using surface plasmon maps obtained via

1 STEM-EELS. Moreover, the plasmonic properties of the Au/SiO₂ nanostructures were obtained using
2 both theoretical calculations and laser irradiation experiments, and the results were compared. Finally,
3 the 3D surface plasmon distribution of them was obtained by using a combination of the plan view
4 and the cross-sectional experiments. The results in this study can therefore facilitate understanding of
5 the dynamics of the NP arrays induced by laser irradiation and reveal new technology that can be
6 used to control the arrays and the plasmonic properties of Au NPs for future development of advanced
7 optical devices.

8

9 **Acknowledgments**

10 The authors thank Mr. K. Ohkubo, Mr. T. Tanioka, R. Oota, and Dr. Z. Yang for their technical
11 assistance and helpful discussion. This study was conducted at Hokkaido University, and was
12 supported by the "Nanotechnology Platform" Program of the Ministry of Education, Culture, Sports,
13 Science and Technology (MEXT), Japan (Grant No. HNPA 16_040) and JSPS KAKENHI (Grant No.
14 26420661).

15

16 **AUTHOR INFORMATION**

17 **Corresponding Author**

18 *T. Shibayama shiba@qe.eng.hokudai.ac.jp

19 **Author Contributions**

20 The manuscript was written through contributions of all authors. All authors have given approval to

1 the final version of the manuscript.

2

3

4 **References**

- 5 [1] A. Kiesow, S. Strohark, K. Loschner, A. Heilmann, A. Podlipensky, A. Abdolvand and G. Seifert
6 2005 Generation of wavelength-dependent, periodic line pattern in metal nanoparticle-containing
7 polymer films by femtosecond laser irradiation, *Appl. Phys. Lett.* **86** 153111.
- 8 [2] Y. Yoshida, S. Watanabe, Y. Nishijima, K. Ueno, H. Misawa and T. Kato 2011 Fabrication of a
9 Au/Si nanocomposite structure by nanosecond pulsed laser irradiation, *Nanotechnology.* **22**
10 375607.
- 11 [3] R. Yu, T. Shibayama, X. Meng, S. Takayanagi, Y. Yoshida, S. Yatsu and S. Watanabe 2014 Effects
12 of nanosecond-pulsed laser irradiation on nanostructure formation on the surface of thin Au films
13 on SiO₂ glass substrates, *Appl. Surf. Sci.* **289** 274-280.
- 14 [4] R. Yu, T. Shibayama, X. Meng, S. Takayanagi, S. Yatsu, J. Ishioka and S. Watanabe 2014 Effects
15 of ion and nanosecond-pulsed laser co-irradiation on nanostructure formation on the surface of
16 thin Au films on SiO₂ glass substrates, *J. Appl. Phys.* **115** 143104.
- 17 [5] F. Niekief, P. Schweizer, S. M. Kraschewski, B. Butz and E. Spiecker 2015 The process of solid-
18 state dewetting of Au thin films studied by in situ scanning transmission electron microscopy, *Acta*
19 *Mater.* **90** 118-132.
- 20 [6] J. T. McKeown, N. A. Roberts, J. D. Fowlkes, Y. Wu, T. LaGrange, B. W. Reed, G. H. Campbell
21 and P. D. Rack 2012 Real-time observation of nanosecond liquid-phase assembly of nickel
22 nanoparticles via pulsed-laser heating, *Langmuir* **28** 17168-17175.
- 23 [7] J. T. McKewon, Y. Wu, J. D. Fowlkes, P. D. Rack and G. H. Campbell 2015 Simultaneous in-situ
24 synthesis and characterization of Co@Cu core-shell nanoparticle arrays, *Adv. Mater.* **27** 1060-
25 1065.
- 26 [8] Y. H. Lei, R. X. Yu, T. Shibayama, J. Ishioka, S. Watanabe 2016 In-situ observation of self-
27 assembly of quasi-two-dimensional Au nano-submicron particles on β -SiC substrates via
28 nanosecond-pulsed laser irradiation-induced dewetting of thin Au films, *Mater. Lett.* **164** 202-205.
- 29 [9] Y. Xiang, X. Zhu, Q. Huang, J. Zheng, W. Fu 2015 Real-time monitoring of mycobacterium
30 genomic DNA with target-primed rolling circle amplification by a Au nanoparticle-embedded SPR
31 biosensor, *Biosensors and Bioelectronics.*, **66**, 512-519.
- 32 [10] M. Tahir, B. Tahir, Nor Aishah Saidina Amin 2015 Gold-nanoparticle-modified TiO₂ nanowires

- 1 for plasmon-enhanced photocatalytic CO₂ reduction with H₂ under visible light irradiation, *Appl.*
2 *Surf. Sci.* **356** 1289-1299.
- 3 [11] B. Wu, D. Liu, S. Mubeen, T. T Chuong, M. Moskovits, G. D. Stucky 2016 Anisotropic Growth
4 of TiO₂ onto Gold Nanorods for Plasmon-Enhanced Hydrogen Production from Water
5 Reduction, *J. Am. Chem. Soc.* **138** 1114-1117.
- 6 [12] B. Yu, Y. Zhou, P. Li, W. Tu, P. Li, L. Tang, J. Ye and Z. Zou 2016 Photocatalytic reduction of
7 CO₂ over Ag/TiO₂ nanocomposites prepared with a simple and rapid silver mirror method,
8 *Nanoscale.* **8** 11870-11874.
- 9 [13] H. Dong, Z. Wu, A. El-Shafei, B. Xia, J. Xi, S. Ning, B. Jiao and X. Hou 2015 Ag-encapsulated
10 Au plasmonic nanorods for enhanced dye-sensitized solar cell performance, *J. Mater. Chem. A.*
11 **3** 4659-4668.
- 12 [14] N. Spalatu, J. Hiie, N. Maticiuc, M. Krunk, A. Katerski, V. Mikli, I. Sildos 2015 Plasmonic
13 effect of spray-deposited Au nanoparticles on the performance of CSS CdS/CdTe solar cells,
14 *Appl. Surf. Sci.* **350** 69-73.
- 15 [15] S. Link and M. A. El-Sayed 1999 Size and temperature dependence of the plasmon absorption
16 of colloidal gold nanoparticles, *J. Phys. Chem. B.* **103** 4212-4217.
- 17 [16] K. Lance Kelly, E. Coronado, L. L. Zhao and G. C. Schatz 2003 The optical properties of metal
18 nanoparticles: the influence of size, shape, and dielectric environment, *J. Phys. Chem. B.* **107**
19 668-677.
- 20 [17] W. Rechberger, A. Hohenau, A. Leitner, J. R. Krenn, B. Lamprecht, F. R. Aussenegg 2003
21 Optical properties of two interacting gold nanoparticles, *Optics Communications.* **220** 137-141.
- 22 [18] X. Meng, T. Shibayama, R. Yu, S. Takayanagi, S. Watanabe 2013 Microstructure analysis of ion
23 beam-induced surface nanostructuring of thin Au film deposited on SiO₂ glass, *J. Mater. Sci.* **48**
24 920-928.
- 25 [19] X. Meng, T. Shibayama, R. Yu, S. Takayanagi, S. Watanabe 2013 Shift of localized surface
26 plasmon resonance by Ar-ion irradiation of Ag-Au bimetallic films deposited on Al₂O₃ single
27 crystals, *Nuclear Instruments and Methods in Physics Research B.* **314** 112-116.
- 28 [20] X. Meng, T. Shibayama, R. Yu, S. Takayanagi and S. Watanabe 2013 Ion irradiation synthesis of
29 Ag-Au bimetallic nanospheroids in SiO₂ glass substrate with tunable surface plasmon resonance
30 frequency, *J. Appl. Phys.* **114** 054308.
- 31 [21] X. Meng, T. Shibayama, R. Yu, J. Ishioka and S. Watanabe 2015 Anisotropic surroundings effects
32 on photo absorption of partially embedded Au nanospheroids in silica glass substrate, *AIP*
33 *ADVANCES.* **5** 027112.

- 1 [22] M. Chu, C. Chen, F. Javier Garcia de Abajo, J. Deng and C. Mou 2008 Surface exciton polaritons
2 in individual Au nanoparticles in the far-ultraviolet spectral regime, *Physical Review B*. **77**
3 245402.
- 4 [23] M. Chu, V. Myroshnychenko, C. Chen, J. Deng, C. Mou and F. Javier Garcia de Abajo 2009
5 Probing bright and dark surface-plasmon modes in individual and coupled noble metal
6 nanoparticles using an electron beam, *Nano Lett.* **9**(1) 399-404.
- 7 [24] Ai Leen Koh, Antonio I. Fernandez-Dominguez, David W. McComb, Stefan A. Maier and Joel
8 K. W. Yang 2011 High-resolution mapping of electron-beam-excited plasmon modes in
9 lithographically defined gold nanostructures, *Nano Lett.* **11** 1323-1330.
- 10 [25] Jonathan A. Scholl, Aitzol Garcia-Etxarri, Ai Leen Koh and Jennifer A. Dionne 2013
11 Observation of Quantum tunneling between two plasmonic nanoparticles, *Nano Lett.* **13** 564-
12 569.
- 13 [26] M. Zhao, M. Bosman, M. Danesh, M. Zeng, P. Song, Y. Darma, A. Rusydi, H. Lin, C. Qiu and
14 K. P. Loh 2015 Visible surface plasmon modes in single Bi₂Te₃, *Nano Lett.* **15** 8331-8335.
- 15 [27] F. J. Garcia de Abajo, A. Howie 2002 *Physical Review B*. **65** 115418.
- 16 [28] B. T. Draine and P. J. Flatau, "User guide for the discrete dipole approximation code
17 DDASCAT7.3", 2013. [Online]. Available: <http://arxiv.org/abs/0809.0337>.
- 18 [29] P. J. Flatau and B. T. Draine 2012 Retarded field calculation of electron energy loss in
19 inhomogeneous dielectrics, *Optics express*. **2**(20) 1247-1252.
- 20 [30] P. B. Johnson and R. W. Christy 1972 Optical Constants of the Noble Metals, *Physical review B*.
21 **6**(12) 4370-4379.
- 22 [31] Ahrens, James, Geveci, Berk, Law and Charles, "ParaView: An End-User Tool for Large Data
23 Visualization, Visualization Handbook, Elsevier, 2005, ISBN-13: 978-0123875822." [Online].
24 Available: <http://www.paraview.org/>.
- 25 [32] D. A. Cadenhead and J. F. Danielli 1981 Progress in Surface and Membrane Science, *New York:*
26 *Academic Press, INC.*, pp. 380-469.
- 27 [33] C. V. Thompson, Annu 2012 Solid-state dewetting of thin films, *Rev. Mater. Res.* **42** 399-434.
- 28 [34] S. Yang, F. Xu, S. Ostendorp, G. Wilde, H. Zhao and Y. Lei 2011 Template-confined dewetting
29 process to surface nanopatterns: fabrication, structural tenability, and structure-related properties,
30 *Adv. Funct. Mater* **21** 2446-2455.
- 31 [35] L. Longstreth-Spoor, J. Trice, H. Garcia, C. Zhang and Ramki Kalyanaraman 2006 Nanostructure
32 and microstructure of laser-interference-induced dynamic patterning of Co on Si, *J. Phys. D:*
33 *Appl. Phys.* **39** 5149-5159.

- 1 [36] L. A. Sweatlock, S. A. Maier, H. A. Atwater, J. J. Penninkhof and A. Polman 2005 Highly
2 confined electromagnetic fields in arrays of strongly coupled Ag nanoparticles, *Physical review*
3 *B.* **71** 235408.
- 4 [37] G. Pellegrini, V. Bello, G. Mattei and P. Mazzoldi 2007 Local-field enhancement and plasmon
5 tuning in bimetallic nanoplanets, *Optics express.* **15**(16) 10097-10102.
- 6 [38] C. Chen, J. Wang, F. Tsai, Y. Lu, Y. Kiang and C. Yang 2009 Fabrication of sphere-like Au
7 nanoparticles on substrate with laser irradiation and their polarized localized surface plasmon
8 behaviors, *Optics express.* **17**(16) 14186-14198.
- 9 [39] G. T. Forcherio, P. Blake, M. Seeram, D. Dejarnette and D. K. Roper 2015 Coupled dipole
10 plasmonics of nanoantennas in discontinuous, complex dielectric environments, *Journal of*
11 *quantitative spectroscopy & radiative transfer.* **166** 93-101.
12

1
2
3
4
5
6
7
8
9
10
11
12
13
14
15
16
17
18
19
20
21
22
23

Supporting Information

M1. The video of the laser-induced dewetting was recorded in situ observation running from before irradiation until 600 irradiation pulses using the bottom-mounted charge-coupled device (CCD) camera of the MQB-HVEM at a frame rate of 10 frames per second (HD video software: Gatan DigitalMicrograph, Ver. 2.30.542.0, image resolution: 974×974 pixels, video formats: *.mpeg4).

In this supporting information, the upload video M1 format is convert to *.mpg and the play speed is 64 times faster (Image resolution is convert to 360×360 pixels).

S1. The comparison of different MQB-HVEM images obtained after different numbers of laser pulses.

Image processing

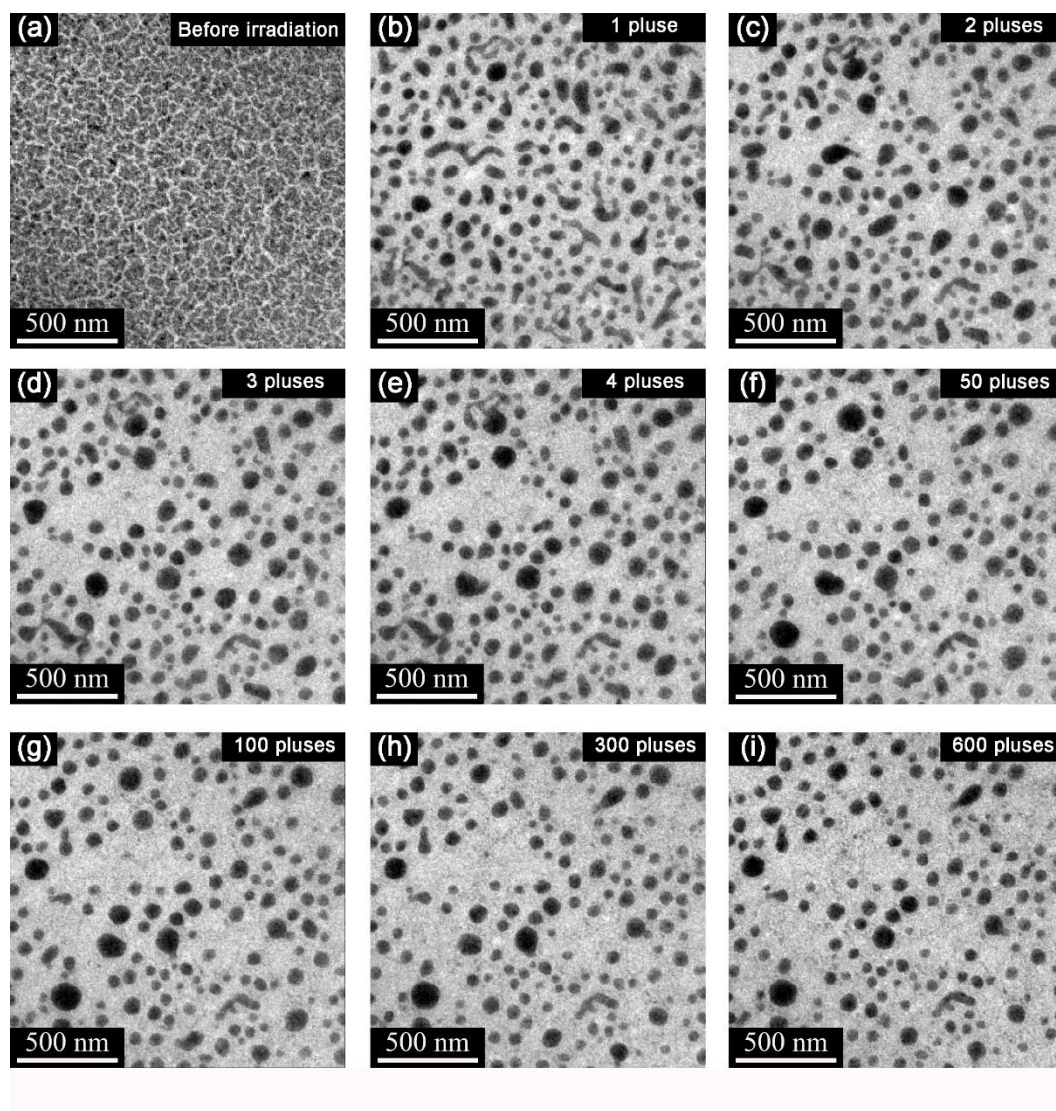
First, each still image was extracted from the movie, where each still image had a resolution of 974×974 pixels with an 8-bit RGB (red-green-blue) color scale. Second, the 8-bit RGB color scale was converted to an 8-bit grayscale. Finally, each still image possessed a resolution of 690×690 pixels after cropping (hereafter referred to as the in situ MQB-HVEM image).

To detect morphological changes and track the individual Au NPs on the SiO₂ glass substrate, the grayscale in situ MQB-HVEM images were converted to exhibit only black for the Au NPs and white for the SiO₂ glass substrate images via a binarization method using Adobe Photoshop CS6. We applied a manual adjustment threshold value for the binarization of each MQB-HVEM image to detect the edge of the Au NPs that was optimized based on visual inspection.

In this in situ observation experiment, the size, shape and distribution of the Au NPs were likely to

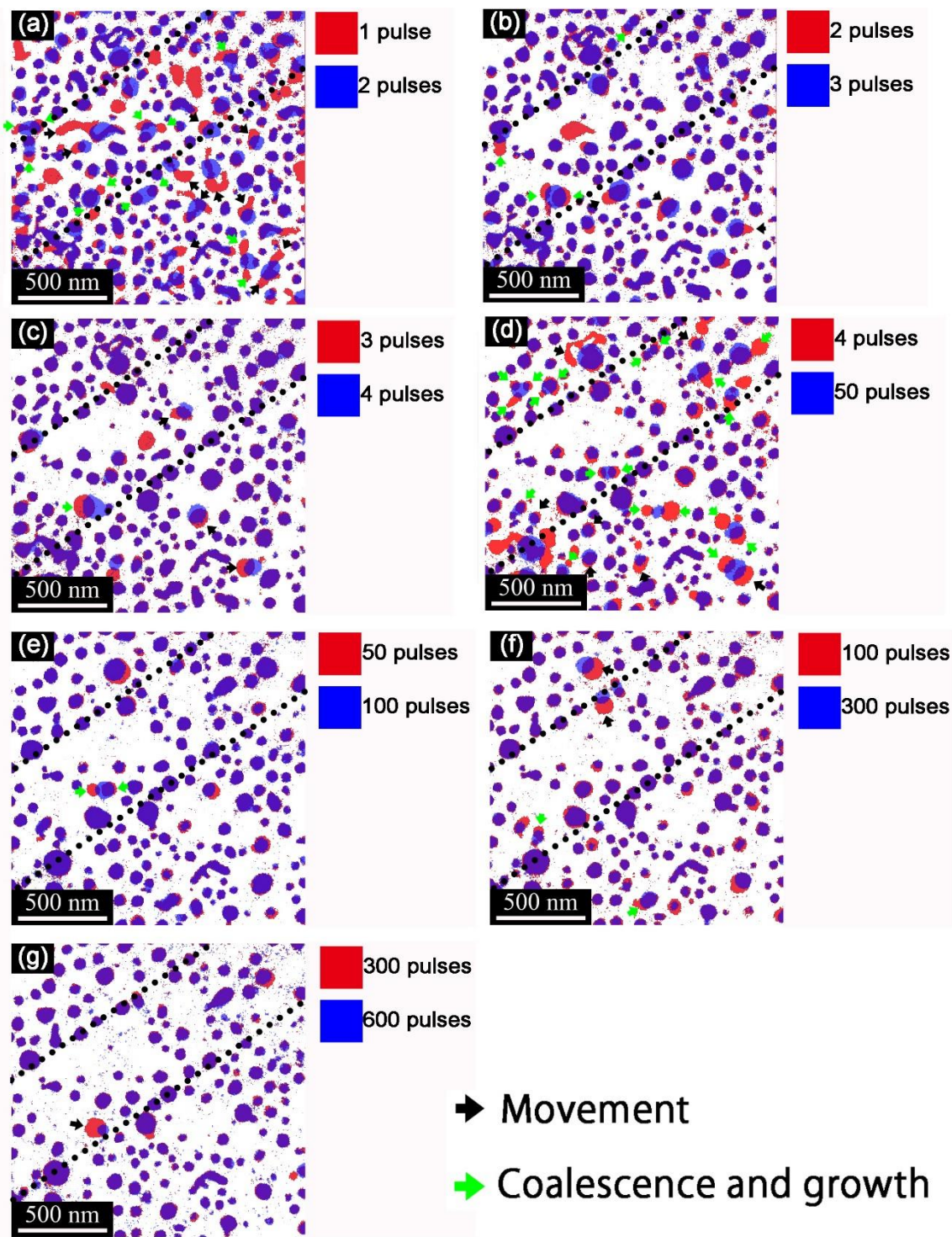
1 be stabilized after 600 irradiation pulses, so we analyzed the movement, coalescence and distribution
2 behavior of the irradiated Au NPs up to this number of pulses. To analyze the behavior, we compared
3 image-processed MQB-HVEM images for a varying number of laser pulses (image processing
4 method given in the experimental procedure). The image position alignment was accomplished using
5 an Au NP present in all of the images that experienced almost no shape change during the in situ
6 observation and that possessed a unique shape resembling the letter 'F' (yellow frame in Figure S1(b)).
7 Figure S1(b)–(i) show the TEM images obtained after 1, 2, 3, 4, 50, 100, 300 and 600 pulses,
8 respectively. Figure S2(a)-(g) show the comparison images between an initial and final image, where
9 the Au NPs appearing in the initial image are colored red and those in the final image are blue. The
10 initial/final comparison images in Figure S2(a)-(g) respectively compare 1 pulse/2 pulses, 2 pulses/3
11 pulses, 3 pulses/4 pulses, 4 pulses/50 pulses, 50 pulses/100 pulses, 100 pulses/300 pulses and 300
12 pulses/600 pulses. Therefore, in the comparison image, blue Au NPs are those that appear after laser
13 irradiation, the red Au NPs are those that have dispersed after laser irradiation, and the red and blue
14 combined (i.e., purple) regions indicates Au NPs that have not changed. In addition, the movement
15 of the Au NPs is indicated by black arrows, while coalesced Au NPs are indicated by green arrows.
16 From 1 to 4 irradiation pulses, some of the Au NPs are seen to have moved to the line-like
17 arrangement of NPs (black dotted line in Figure S2(a)-(g)) and are combined with Au NPs in the
18 neighborhood of the line-like arrangement. Therefore, the number of Au NPs is reduced by the
19 nanosecond-pulsed laser irradiation in the region between the black dotted lines. As shown in Figure
20 2 in the manuscript, several Au NPs are arranged to resemble a line along the yellow dotted lines.
21

1 Figure S1



2 Figure S1. MQB-HVEM images acquired (a) before irradiation and after (b) 1, (c) 2, (d) 3, (e) 4,
3 (f) 50, (g) 100, (h) 300 and (i) 600 irradiation pulses.

1 Figure S2



2 Figure S2. Comparison images of initial/final images comparing (a) 1 pulse/2 pulses, (b) 2 pulses/3

1 pulses, (c) 3 pulses/4 pulses, (d) 4 pulses/50 pulses, (e) 50 pulses/100 pulses, (f) 100 pulses/300 pulses
2 and (g) 300 pulses/600 pulses. In the comparison images (a)-(g), the Au NPs appearing in the initial
3 image are colored red and those in the final image are blue.
4

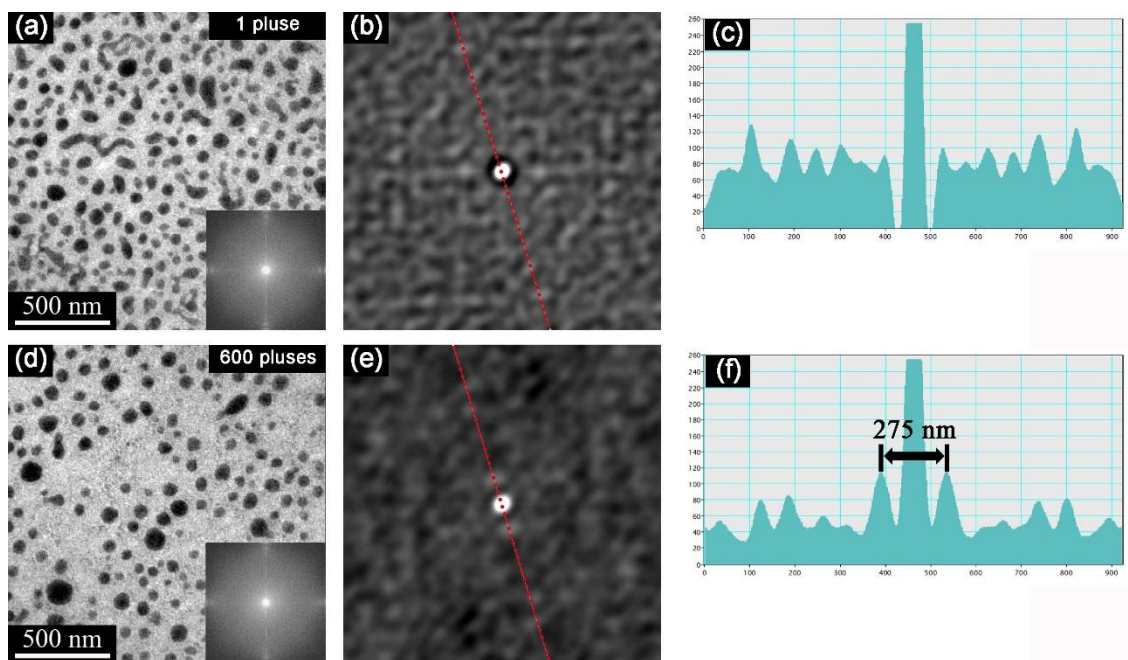
1 S2. Fast Fourier transform (FFT) analysis of the Au NPs distribution after laser irradiation.

2

3 Figure S3 shows MQB-HVEM images of (a) after 1 irradiation pulse and (d) after 600 irradiation
4 pulses, lower right inset of (a) and (d) the corresponding fast Fourier transform (FFT) patterns,
5 respectively. Figure S3 (b) and (e) show the autocorrelation functional (ACF) image obtained by FFT
6 patterns in Figure S3 (a) and (d), respectively. Figure S3(c) and (f) show the line profiles in the
7 direction of red dotted line as shown in Figure S3 (b) and (e), respectively. After 600 irradiation pulses,
8 bright pair dots are appeared in the ACF image (Figure S3 (e)) and the distance between the bright
9 dots are about 275 nm in the line profiles image (Figure S3 (f)). These results indicate that the
10 distribution of the Au NPs began to evolve in a line arrangement. Moreover, the direction of several
11 Au NPs movement is toward the yellow dotted line as shown in Figure 2 and Figure S2.

12

1 **Figure S3**



2 **Figure S3.** MQB-HVEM images of (a) after 1 irradiation pulse and (d) after 600 irradiation pulses,
3 lower right inset of (a) and (d) the corresponding fast Fourier transform (FFT) patterns, respectively,
4 (b) and (e) the autocorrelation functional (ACF) image obtained by FFT patterns in (a) and (d),
5 respectively.